

RESEARCH ARTICLE

10.1002/2014WR016816

Control of coupling mass balance error in a process-based numerical model of surface-subsurface flow interaction

Marcello Fiorentini¹, Stefano Orlandini¹, and Claudio Paniconi²

¹Dipartimento di Ingegneria Enzo Ferrari, Università degli Studi di Modena e Reggio Emilia, Modena, Italy, ²Institut National de la Recherche Scientifique, Centre Eau Terre Environnement (INRS-ETE), Quebec City, Canada

Key Points:

- Coupling mass balance error in a surface-subsurface flow model is investigated
- Time step control based on a degree of coupling index is proposed and tested
- The interpolation algorithm used to pass exchange variables is improved

Correspondence to:

S. Orlandini,
stefano.orlandini@unimore.it

Citation:

Fiorentini, M., S. Orlandini, and C. Paniconi (2015), Control of coupling mass balance error in a process-based numerical model of surface-subsurface flow interaction, *Water Resour. Res.*, 51, 5698–5716, doi:10.1002/2014WR016816.

Received 17 DEC 2014

Accepted 28 JUN 2015

Accepted article online 2 JUL 2015

Published online 26 JUL 2015

Abstract A process-based numerical model of integrated surface-subsurface flow is analyzed in order to identify, track, and reduce the mass balance errors affiliated with the model's coupling scheme. The sources of coupling error include a surface-subsurface grid interface that requires node-to-cell and cell-to-node interpolation of exchange fluxes and ponding heads, and a sequential iterative time matching procedure that includes a time lag in these same exchange terms. Based on numerical experiments carried out for two synthetic test cases and for a complex drainage basin in northern Italy, it is shown that the coupling mass balance error increases during the flood recession limb when the rate of change in the fluxes exchanged between the surface and subsurface is highest. A dimensionless index that quantifies the degree of coupling and a saturated area index are introduced to monitor the sensitivity of the model to coupling error. Error reduction is achieved through improvements to the heuristic procedure used to control and adapt the time step interval and to the interpolation algorithm used to pass exchange variables from nodes to cells. The analysis presented illustrates the trade-offs between a flexible description of surface and subsurface flow processes and the numerical errors inherent in sequential iterative coupling with staggered nodal points at the land surface interface, and it reveals mitigation strategies that are applicable to all integrated models sharing this coupling and discretization approach.

1. Introduction

Several process-based catchment-scale hydrologic models have been developed in recent years to describe the coupling (i.e., interactions and feedbacks) between the surface and subsurface components of the water cycle [Kampf and Burges, 2007; Furman, 2008; Maxwell et al., 2014]. As in any numerical modeling of coupled phenomena, a choice is made between sequential (or asynchronous), sequential iterative, and full coupling approaches, with pros and cons for each approach that reflect efficiency, accuracy, and other performance considerations. In surface-subsurface flow modeling, sequential coupling is used, for instance, in the models developed by Ivanov et al. [2004] and Shen and Phanikumar [2010], sequential iterative coupling in the models of Camporese et al. [2010] and Delfs et al. [2009], and full coupling in the models of Kollet and Maxwell [2006], Panday and Huyakorn [2004], and Aricó et al. [2011]. Recent intercomparison studies have examined the trade-offs of both sequential and full coupling [Ebel et al., 2009; Sulis et al., 2010; Liggett et al., 2012; Sebben et al., 2013; Maxwell et al., 2014].

Mathematically, the coupling can be expressed in terms of first-order exchange [VanderKwaak and Loague, 2001; Panday and Huyakorn, 2004], continuity of pressure [Kollet and Maxwell, 2006], or a boundary condition switching procedure [Camporese et al., 2010]. The representation and resolution of exchange or coupling terms will introduce errors that can affect numerical performance. The discrepancy of model results from perfect closure of the water mass balance can be used as an indicator of model performance and suitability [Freeze and Harlan, 1969]. Coupling mass balance errors have been evaluated in Dagès et al. [2012] for a sequential iterative model, but the problem of controlling (tracking and reducing) coupling mass balance errors in detailed surface-subsurface flow models has not been specifically addressed so far.

An in-depth analysis of the sources of mass balance error is presented in this paper by considering the CATHY (CATchment HYdrology) model described in Camporese et al. [2010] that features sequential iterative coupling with staggered nodal points at the land surface interface. In CATHY, local contributions to surface flow propagation are computed using a cell-centered scheme based on the grid digital elevation model

describing the land surface topography [Orlandini and Moretti, 2009; Orlandini et al., 2014], while subsurface flow propagation is described using a mesh of tetrahedra built by subdividing the grid cells of the digital elevation model into triangles [Paniconi and Putti, 1994]. This design facilitates a flexible description of surface and subsurface flow processes that are inherently different. However, since the discretized computational domains at the land-atmosphere interface require node-to-cell and cell-to-node interpolation algorithms to pass from surface to subsurface variables, and vice versa, the coupling scheme can be a source of error, as shown by Goumiri and Prevost [2011] for reservoir simulation models. A second source of coupling error in the CATHY model is in the sequential iterative procedure that solves the surface flow routing with a time-explicit scheme and the subsurface equation with a time-implicit, iterative scheme. Due to these different temporal schemes, exchange fluxes between the surface and subsurface compartments are not completely synchronous, and errors can be introduced.

The aims of this study are to provide an in-depth mass balance analysis of the sources of coupling error in the CATHY model, to introduce metrics that can signal when a simulation is liable to generate high errors, and to propose improvements to coupling related algorithms in the model. Temporal and spatial patterns of mass balance error are examined by using dimensionless global indices that synthesize the dynamics of the simulated processes and the related behavior of the numerical model. Specifically, a saturated area index and a degree of coupling index are introduced to help monitor the interpolation and time stepping errors. The analyses are conducted for two synthetic test cases, a sloping plane and a tilted v-catchment, and for the Enza River drainage basin in northern Italy. Numerical performance of the model, of the dimensionless indices, and of the improved schemes is assessed for varying time step sizes and horizontal mesh resolutions.

2. Surface-Subsurface Flow Coupling

Integrated models of drainage basin hydrology developed by coupling a three-dimensional (3-D) subsurface flow model with a quasi-2-D surface flow propagation model are essential diagnostic tools for advancing our understanding of complex hydrologic fluxes at the land-atmosphere interface [Freeze and Harlan, 1969; Camporese et al., 2010; Weill et al., 2013; Niu et al., 2014]. They can be used for instance to predict the response of drainage basins to climate forcing in long-term hydrologic simulations since they are able to resolve the various surface runoff generation mechanisms (Horton, Dunne, return flow) that may occur across different land surface, land use, and climate conditions [Maxwell and Miller, 2005; Sulis et al., 2011]. The CATHY model simulates surface and subsurface water flows by coupling a 3-D solver of Richards' equation for variably saturated porous media with a path-based grid network solver of the diffusion wave equation [Paniconi and Wood, 1993; Orlandini and Rosso, 1998; Camporese et al., 2010]. The coupled hydrological problem is described by two differential equations, namely

$$S_s S_w(\psi) \frac{\partial \psi}{\partial t} + \phi \frac{\partial S_w}{\partial t} = \nabla \cdot (K_r(\psi) K_s(\nabla \psi + \boldsymbol{\eta}_z)) + q_{ssw}(h, \psi) \quad (1)$$

and

$$\frac{\partial Q}{\partial t} + c_k(Q) \frac{\partial Q}{\partial s} = D_h(Q) \frac{\partial^2 Q}{\partial s^2} + c_k(Q) q_L(h, \psi). \quad (2)$$

In the subsurface flow equation (1), S_s (L^{-1}) is the specific storage term, $S_w(\psi)$ (-) is the water saturation, ψ (L) is the pressure head, t (t) is time, ϕ (-) is the porosity, ∇ (L^{-1}) is the gradient operator, $K_r(\psi)$ (-) is the relative hydraulic soil conductivity function, K_s ($L t^{-1}$) is the saturated hydraulic conductivity tensor, $\boldsymbol{\eta}_z = (0, 0, 1)^T$ (the vertical coordinate is positive upward), and q_{ssw} (t^{-1}) is a surface-to-subsurface exchange term (rate per unit volume) that depends on surface ponding head h (L) and pressure head ψ . In the surface flow equation (2), Q ($L^3 t^{-1}$) is the discharge along the overland/channel link, c_k ($L t^{-1}$) is the kinematic wave celerity, s (L) is the spatial coordinate along the drainage network, D_h ($L^2 t^{-1}$) is the hydraulic diffusivity, and q_L ($L^2 t^{-1}$) is the lateral inflow from the subsurface to the surface (negative if outflow). The CATHY model uses a finite element method to solve the Richards equation and a finite difference method for the hillslope and channel routing equation [Camporese et al., 2010]. The surface module solves the diffusion wave equation along a complex network of rivulets and channels obtained by processing grid-based digital elevation models [Orlandini and Rosso, 1998; Orlandini and Moretti, 2009; Orlandini et al., 2012]. Local

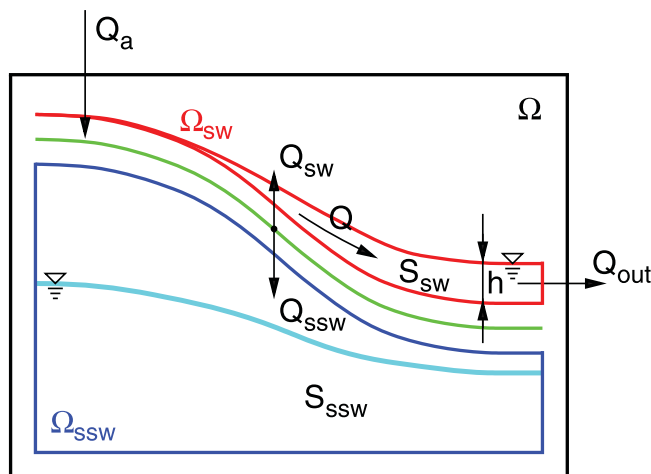


Figure 1. Sketch of the principal variables processed by the CATHY model. The external black box defines the control volume of the whole domain, the red and blue lines show the limits of the surface and subsurface compartments, respectively, and the green line describes the interface internal boundary between the surface and subsurface domains.

water storage, S (L^3), is defined by the contributions of the surface water storage S_{SW} (L^3) and the subsurface water storage, S_{SSW} (L^3). The external inflows in Ω are defined by the volumetric flow rate given by the atmospheric forcing Q_a ($L^3 t^{-1}$), while outflows are defined by the hydrograph from the outlet Q_{out} ($L^3 t^{-1}$). Lateral inflows and outflows and sink terms for the subsurface compartment can be handled by CATHY [Camporese et al., 2010], but are not considered for the error analysis reported in this paper.

CATHY implements a sequential iterative coupling scheme that solves in cascade the surface and subsurface water flow as sketched in Figure 2. A boundary condition switching procedure manages the exchange of information between Ω_{SW} and Ω_{SSW} by partitioning the atmospheric forcing flow rate Q_a into a volumetric flow rate to the surface Q_{SW} ($L^3 t^{-1}$) and to the subsurface Q_{SSW} ($L^3 t^{-1}$). The volumetric flow rate to the surface Q_{SW} is then interpolated to q_L ($L^2 t^{-1}$) and used as lateral inflow contribution in solving the surface flow

contributions to surface flow propagation are computed by using a cell centered scheme based on the grid digital elevation model of the land surface. The mesh for the subsurface flow solver is based on tetrahedral elements that, for the surface-most layer, are built from the vertices of the surface cells. The surface-subsurface mesh therefore requires a specific procedure to pass information regarding interactions and feedbacks between the cell-based surface and node-based subsurface compartments.

As shown in Figure 1, the general scheme for a drainage basin model in CATHY is defined by the coupled surface-subsurface domain Ω and its subdomains: the surface Ω_{SW} and subsurface Ω_{SSW} compartments. The total

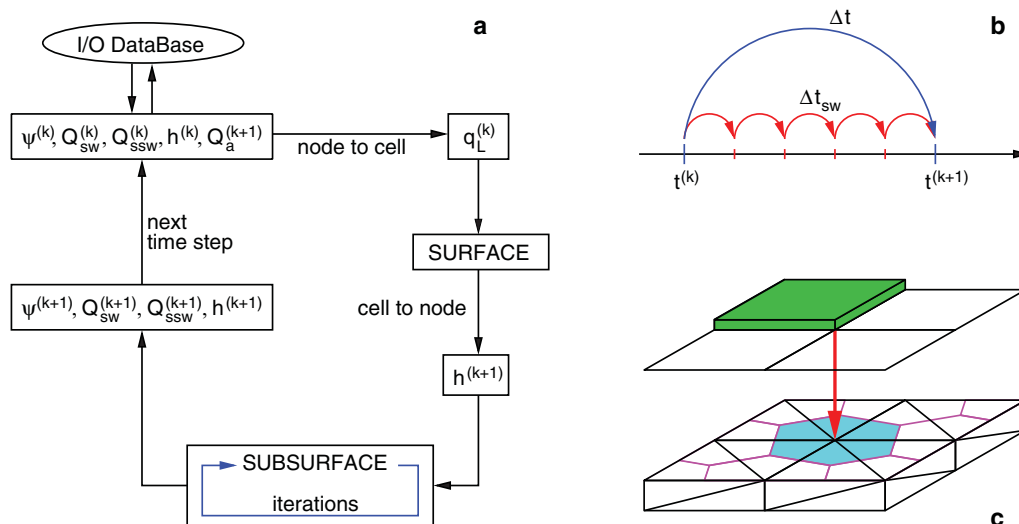


Figure 2. Sketch of the surface-subsurface interaction algorithm performed by CATHY. The algorithm is shown in (a). The surface time substepping used for surface routing is shown in (b). The coupling geometry adopted in CATHY is represented in (c) where the surface domain is described with a raster-based configuration (top) connected with the subsurface compartment characterized by a tetrahedral geometry (bottom).

equation (2), whereas Q_{ssw} is used as atmospheric boundary conditions for the subsurface flow equation (1) [Camporese et al., 2010].

2.1. Information Passing

The switching procedure is nested in the subsurface flow solver and it is performed for land surface nodes in which, by looking from the current time level k to the next time level $k + 1$, the potential atmospheric forcing $Q_a^{(k+1)}$ ($L^3 t^{-1}$) is partitioned into a volumetric flow rate to the surface $Q_{sw}^{(k+1)}$ and to the subsurface $Q_{ssw}^{(k+1)}$ compartments by imposing

$$Q_{sw}^{(k+1)} = Q_a^{(k+1)} - Q_{ssw}^{(k+1,r)}, \tag{3}$$

where r is the counter for the nonlinear iterations in the subsurface solver. The atmospheric forcing $Q_a^{(k+1)}$ is assumed to be positive for rainfall and negative for potential evaporation, the volumetric flow rate to the subsurface $Q_{ssw}^{(k+1)}$ is assumed to be positive for infiltration and negative for exfiltration, and the volumetric flow rate to the surface $Q_{sw}^{(k+1)}$ is positive for runoff or return flow and negative for evaporation or infiltration losses. The volumetric flow rate to the subsurface is estimated at each iteration r by the subsurface flow solver by imposing a Neumann boundary condition or by back-calculating Q_{ssw} from a Dirichlet boundary condition at a saturated node [Camporese et al., 2010; Dagès et al., 2012; Camporese et al., 2014]. Considering that the surface routing represented by equation (2) is solved by a time-explicit Muskingum-Cunge scheme and it is solved before the Richards solver, the estimation of the distributed lateral term q_L is computed at time $t^{(k)}$. The volumetric flow rate to the surface $Q_{sw}^{(k)}$ calculated at time level k needs to be linearly interpolated from nodes to cells. The obtained distributed lateral inflow on cells $q_L^{(k)}$ is then used in the surface flow module to estimate the outflow discharge from each surface cell with the Muskingum-Cunge method [Orlandini and Rosso, 1996]. The storage equation associated to the i th cell

$$\frac{dS_{sw}^{(i)}}{dt} = J^{(i)}(t) - O^{(i)}(t) + q_L^{(i)} \Delta s^{(i)}, \tag{4}$$

where $S_{sw}^{(i)}$ (L^3) is the storage on the current surface cell i , $J^{(i)}$ ($L^3 t^{-1}$) is the inflow discharge from the upstream drainage basin, $O^{(i)}$ ($L^3 t^{-1}$) is the downstream outflow discharge, $q_L^{(i)}$ ($L^2 t^{-1}$) is the lateral inflow contribution, and $\Delta s^{(i)}$ (L) is the link length, is then solved numerically to compute the current cell surface water storage. The trapezoidal integration rule is used to discretize the storage equation. Surface cell storage terms are then linearly interpolated from cell to nodes to obtain the ponding heads $h^{(k+1)}$ (L) at time level $k + 1$.

2.2. Time Stepping

The solution of the coupled hydrological problem is driven by the subsurface flow solver. Thus, the time step adaptation strategy is managed via a classical heuristic algorithm that scales the time interval on the basis of the number of nonlinear iterations that were needed to solve the current time step

$$\Delta t^{(k+1)} = \begin{cases} m_m \Delta t^{(k)} + a_1 & R < R_1 \\ \Delta t^{(k)} & R_1 \leq R < R_2 \\ m_r \Delta t^{(k)} - a_2 & R \geq R_2 \end{cases}, \tag{5}$$

where m_m (> 1) and m_r (< 1) ($-$) are scaling coefficients, a_1 and a_2 (t) are, respectively, additive and subtractive terms, R is the total number of nonlinear iterations needed to achieve convergence, and R_1 and R_2 are the lower and upper threshold iteration values, respectively. The time step size Δt can assume values ranging between Δt_{min} and Δt_{max} , user-defined the minimum and maximum time step sizes, respectively.

A time substepping for the surface routing is also performed in order to ensure that the Courant number Cu is approximately equal to 1 so that the accuracy requirements of the Muskingum-Cunge method are met [Ponce, 1986; Syriopoulou and Koussis, 1991; Orlandini and Rosso, 1996]. The maximum Courant number is calculated for the whole water basin at the previous time level (k), namely

$$Cu_{max}^{(k)} = \max(c_k / \Delta s) \Delta t^{(k)}. \tag{6}$$

When Cu_{max} exceeds the threshold value $Cu_t=1$, a time substepping is performed at the next time level $t^{(k+1)}$ by setting the number of surface time substeps as

$$n_{sts} = \text{ceiling}(Cu_{max}/Cu_t) \quad (7)$$

so that the surface time step size becomes

$$\Delta t_{sw} = \Delta t / n_{sts}. \quad (8)$$

As sketched in Figure 2b, the surface routing is nested into the subsurface time step size Δt , thus it is solved in cascade n_{sts} times without recalculating the volumetric flow rate terms at every surface time substep.

3. Mass Balance Errors

As shown in Figure 1, the water mass balance is performed by using the control volume Ω for the whole drainage basin, the control volume Ω_{sw} for the surface compartment, and the control volume Ω_{ssw} for the subsurface compartment. The analysis is developed by integrating over time the fluxes Q shown in Figure 1. In volumetric terms, the cumulative global water balance error in the drainage basin at time level $k + 1$ can be defined as

$$\epsilon^{(k+1)} = V_a^{(k+1)} - V_{out}^{(k+1)} - \Delta S_{ssw}^{(k+1)} - \Delta S_{sw}^{(k+1)}, \quad (9)$$

where $V_a^{(k+1)}$ (L^3) is the net atmospheric volume that has entered (positive) or exited (negative) Ω from time zero to time $t^{(k+1)}$, $V_{out}^{(k+1)}$ (L^3) is the net surface flow volume from the outlet cell, $\Delta S_{ssw}^{(k+1)}$ (L^3) represents the groundwater storage variation from initial conditions to the current time, and $\Delta S_{sw}^{(k+1)}$ (L^3) is the difference between the current and initial state of surface water storage. The cumulative surface water mass balance error at time $t^{(k+1)}$ is given by

$$\epsilon_{sw}^{(k+1)} = V_{sw}^{(k)} - V_{out}^{(k+1)} - \Delta S_{sw}^{(k+1)}, \quad (10)$$

where $V_{sw}^{(k)}$ (L^3) is the net exchange volume to the surface compartment considered positive for runoff and return flow gains and negative for evaporation and infiltration losses. It is evaluated at time level k because of the time-explicit solution of surface routing within a sequential coupling procedure, as explained earlier. For the surface domain, it is possible to define also the specific cell surface error at the current time step $k + 1$ by using the trapezoidal rule on equation (4) for every cell i

$$\epsilon_{cell}^{(k+1,i)} = \left(\frac{f^{(k,i)} + f^{(k+1,i)}}{2} \Delta t - \frac{O^{(k,i)} + O^{(k+1,i)}}{2} \Delta t + q_L^{(k,i)} \Delta S^{(i)} \Delta t - S_{sw}^{(k+1,i)} + S_{sw}^{(k,i)} \right) / \Delta x^2, \quad (11)$$

where Δx is the surface grid cell size (L). The cumulative subsurface mass balance error is then defined as

$$\epsilon_{ssw}^{(k+1)} = V_{ssw}^{(k+1)} - \Delta S_{ssw}^{(k+1)}, \quad (12)$$

where $V_{ssw}^{(k+1)}$ is the net exchange volume to the subsurface compartment (positive for infiltration, negative for exfiltration). Finally, the cumulative mass balance error due to the coupling scheme can be computed as the residual between the global mass error ϵ and the sum of subsurface and surface errors [Dagès et al., 2012], that is

$$\epsilon_c^{(k+1)} = \epsilon^{(k+1)} - \epsilon_{ssw}^{(k+1)} - \epsilon_{sw}^{(k+1)}. \quad (13)$$

The coupling water balance error $\epsilon_c^{(k+1)}$ is zero if the surface and subsurface modules are well integrated and the exchange of information is perfectly managed.

3.1. Sources of Coupling Error

The coupling error in the CATHY model is investigated by focusing on two different sources of this error: (1) the time stepping scheme and (2) the interpolation algorithm used in exchanging information between the surface and subsurface compartments.

3.1.1. Time Stepping Scheme

The time stepping scheme described earlier solves the surface routing equation by using the volumetric flow rate to the surface $Q_{sw}^{(k)}$ calculated at the time step $t^{(k)}$ [Dagès et al., 2012]. Meanwhile, the subsurface

flow equation is solved by using the new values volumetric flow rate to the subsurface $Q_{SSW}^{(k+1,r)}$ at time level $t^{(k+1)}$ and iteration r . By substituting equations (9), (10), and (12) into equation (13), the coupling error can be rewritten as

$$\epsilon_c^{(k+1)} = V_a^{(k+1)} - V_{SW}^{(k)} - V_{SSW}^{(k+1)}. \tag{14}$$

The mismatch or lag between $Q_{SW}^{(k)}$ and $Q_{SSW}^{(k+1)}$ thus contributes in a direct way to the coupling error via the computation of their integrals $V_{SW}^{(k)}$ and $V_{SSW}^{(k+1)}$. The magnitude of this error will be in part dependent on the time step sizes used in the sequential iterative solution procedure.

3.1.2. Interpolation Algorithm

The volumetric flow rate to the surface Q_{SW} is calculated in the switching procedure by imposing continuity through equation (3). The interpolation from Q_{SW} to q_L filters spatial patterns over two dimensions laterally without considering the effective availability of water on surface cells. This procedure can have significant effects on mass balance error as sketched in Figure 2c. The reference area of each node, used to estimate fluxes for the subsurface compartment, is delineated by magenta lines, while the cyan area depicts the reference area of the central node (Figure 2c). For the central surface node in Figure 2c, the subsurface flow solver can evaluate an infiltration volumetric flow rate Q_{SW} from the surface to the subsurface domain (red arrow in Figure 2c). This value is negative and it is partitioned over each cell j that belongs to the node considered, but some surface cells may not actually be in a saturated state, as depicted in the example shown in Figure 2c with three unsaturated surface cells. The current interpolation scheme calculates a lateral contribution $q_{L,j}$ ($L^2 t^{-1}$) for every cell j and this is used in the wave propagation on the surface domain. Some cells may have sufficient surface water storage (the green solid in Figure 2c) for routing, while other cells do not have surface water storage consistent with the lateral outflow calculated by the linear node-to-cell interpolation. Since the spatial interpolation adopted is geometrical, it does not follow the distribution and availability of surface water storage, thus the surface error ϵ_{SW} increases if a negative value of $q_{L,i}$ is calculated where no water is available to infiltrate or evaporate. This error is computed as part of the surface error ϵ_{SW} , but it is conceptually connected to an exchange error in surface-subsurface water interaction.

3.2. Controlling the Coupling Errors

3.2.1. Saturation and Coupling Indices

Mass balance errors can be controlled by using two normalized indices that track the fraction of saturated area over the drainage basin and the degree of coupling between the surface and subsurface modules. The total saturated area index was defined by Weill *et al.* [2013], as

$$SI = A_{sat} / A_b, \tag{15}$$

where A_{sat} is the area of the land surface that is saturated at the current time step (L^2) and A_b is the total area of the drainage basin (L^2).

The degree of coupling is based on the relative volume of surface-subsurface exchange that occurs on saturated portions of the catchment, and is defined as

$$CI = \begin{cases} (V_{in}^{(SA)} + V_{ex}^{(SA)}) / (V_{in} + V_{ex}) & Q_a \neq 0 \\ SI & Q_a = 0 \end{cases}, \tag{16}$$

where V_{in} and V_{ex} are the total infiltration and exfiltration volumes across the soil surface at the current time step, respectively, and $V_{in}^{(SA)}$ and $V_{ex}^{(SA)}$ are the total infiltration and exfiltration volumes across surface saturated nodes, respectively. When $CI=0$, there is no surface saturation, and therefore no surface routing, so the model is effectively decoupled (only the subsurface module is active). When $CI=1$, the surface and subsurface compartments are fully interacting over the entire drainage basin.

3.2.2. A Modified Time Step Adaptation Scheme

When the coupling index is changing rapidly during the simulation, there are high variations in volumetric flow rate to the surface and subsurface compartments and consequently strong dynamics on the catchment. This information can be used to improve the adaptive time stepping algorithm used in CATHY. The normalized variation of the coupling index can be written as

$$W_{CI}^{(k+1)} = \left| 1 - \frac{CI^{(k)}}{CI^{(k+1)}} \right|, \quad (17)$$

The adaptive time stepping scheme given in equation (5) is modified to

$$\Delta t^{(k+1)} = \begin{cases} (m_m - W_{CI}^{(k+1)}) \Delta t^{(k)} + a_1 & R < R_1 \\ \min(1, m_m - W_{CI}^{(k+1)}) \Delta t^{(k)} & R_1 \leq R < R_2, \\ (m_r - W_{CI}^{(k+1)}) \Delta t^{(k)} - a_2 & R \geq R_2 \end{cases}, \quad (18)$$

3.2.3. A Modified Node-to-Cell Passing Algorithm

The linear interpolation scheme in CATHY for passing the volumetric flow rate to the surface, Q_{sw} , defined on surface nodes, to the lateral contribution variable, q_L , defined on the i th surface cell, is given by

$$q_L^{(k,i)} = \frac{1}{4\Delta s^{(i)}} \sum_{j=1}^4 Q_{sw}^{(k,j)}, \quad (19)$$

where j is a counter for the four nodes that belong to cell i . The new approach considers the effective availability of surface water storage in partitioning the volumetric flow rate to the surface from nodes to cells. When Q_{sw} is negative (loss of water from the surface domain due to infiltration or evaporation) and the inflow released from upstream cells is null, at time levels $t^{(k+1)}$ and $t^{(k)}$, the modified algorithm uses the formula

$$q_L^{(k,i)} = \begin{cases} \frac{1}{4\Delta s^{(i)}} \sum_{j=1}^4 Q_{sw}^{(k,j)} w_j, & \text{if } S^{(k,i)} > 0 \\ 0, & \text{if } S^{(k,i)} = 0 \end{cases}, \quad (20)$$

where w_j (-) is a weight factor defined as

$$w_j = N_j / N_j^{(S)}, \quad (21)$$

with N_j and $N_j^{(S)}$, respectively the number of cells and the number of saturated cells connected with the j th node. The weight coefficient w_j preserves a linear interpolation if all cells that belong to the current node j are saturated, it is greater than 1 if one or more cells are unsaturated and cell i is a saturated cell, and it is equal to 0 if cell i is unsaturated. In this way, considering the case depicted in Figure 2c as an example, the infiltration flux estimated on the central node (red arrow) is partitioned only to one cell, thus the negative volumetric flow rate is associated only to saturated cells and the contribution of nodal values to q_L is null for unsaturated cells.

4. Numerical Experiments

Two synthetic test cases, a sloping plane and a tilted v-catchment [Sulis et al., 2010; Maxwell et al., 2014], and a real case study, the Enza River drainage basin, were used to analyze coupling mass balance errors and to test the proposed indices and modified algorithms. The representation of 3-D geometry of surface and subsurface compartments implemented in CATHY for the test cases is shown in Figure 3. The geometric properties of the synthetic test cases are reported in Table 1. The parameter values considered in the test cases are reported in Table 2. Special attention has been paid in the present investigation to the grid cell size used to discretize planimetrically the drainage system. The role of the vertical discretization of the subsurface domain was investigated by Dagès et al. [2012]. The Enza River drainage basin is located in northern Italy, its drainage area is 463 km², the latitude and longitude of its centroid are 44° 27' 5.22" N and 14° 17' 25.67" E, and the terrain elevation ranges between 202 and 1963 m asl (Figure 3c). For all the considered drainage systems, the D8-LTD algorithm was applied to build the grid and channel networks along which surface runoff propagates [Orlandini et al., 2003].

In all test cases, the van Genuchten soil retention curve [van Genuchten and Nielsen, 1985] was used with parameters corresponding to a sandy-loam soil ($\alpha=1.0 \text{ m}^{-1}$, $n=2.0$, $\theta_r=0.08$, and $\theta_s=0.40$). The initial

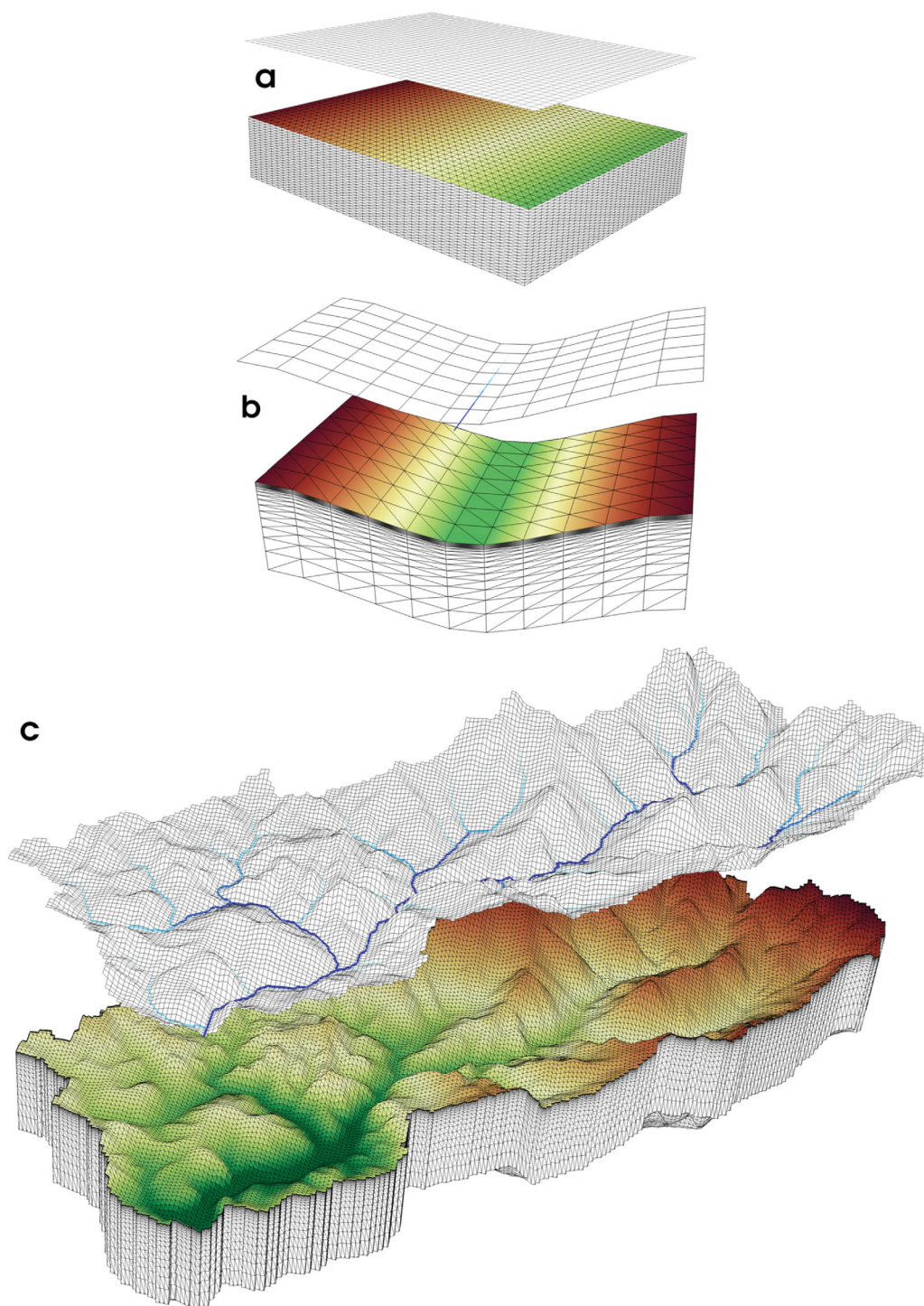


Figure 3. Three-dimensional representations of the surface and subsurface domains for the three test cases: (a) sloping plane based on a 10 m DEM, (b) tilted v-catchment based on a 75 m DEM, and (c) Enza River drainage basin based on a 180 m DEM.

condition was imposed by considering a vertical hydrostatic pressure distribution. The initial time step size was set to 1 s in order to assure convergence and coherence between numerical simulations. The convergence criteria consisted of a tolerance of 0.005 m calculated for the pressure terms on a Euclidean norm, a maximum number of iterations of 15, and a minimum time step size of 1 s. The synthetic test cases were forced with a single rainfall period followed by a drainage or evaporation period, whereas the Enza River

Table 1. Geometric Parameter Values for the Synthetic Test Cases

Variable	Units	Sloping Plane	Tilted v-Catchment	
			Planes	Valley
Length	m	400	375	525
Width	m	320	525	75
x direction slope	%	0.05	10	0
y direction slope	%	0	0	2

case study was subjected to a seasonal forcing composed of two wet periods alternated by two dry seasons. The characteristic values of atmospheric forcing are reported in Table 2 and a plot of the atmospheric forcing boundary conditions is displayed in Figure 4, where an example of the hydrologic response for each of the three test cases is shown. The sloping plane response in this example was obtained using a time step size of 15 s and a horizontal grid cell size resolution of 10 m (Figures 4a and 4b), the tilted v-catchment response was simulated using a time step size of 30 s and a horizontal grid cell size of 75 m (Figures 4c and 4d), and the Enza River drainage basin response was obtained using a time step size of 1800 s and a horizontal grid cell size of 180 m (Figures 4e and 4f).

5. Results

The mass balance behavior is investigated by monitoring the simulated temporal and spatial patterns of subsurface, surface, and coupling errors. In the numerical experiment results, the different sources of coupling error will first be shown, followed by a demonstration of the proposed indices in tracking this error, and finally the performance of the modified interpolation and time stepping schemes in reducing mass balance errors will be assessed. The total volumes of net atmospheric forcing (rainfall minus evaporative demand) involved in the simulations are 8448 m³, 26178 m³, and 4.96 × 10⁷ m³ for the sloping plane, tilted v-catchment, and Enza River drainage basin, respectively. The maximum ranges observed in the simulated subsurface water storage are about 3186 m³, 5128 m³, and 1.38 × 10⁸ m³ for the sloping plane, tilted v-catchment, and Enza River drainage basin, respectively. The maximum ranges in the simulated surface water storage are about 3310 m³, 8607 m³, and 7.71 × 10⁵ m³, respectively, for these three test cases.

5.1. Sources of Coupling Error

5.1.1. Time Stepping Scheme

The results highlight a strong influence of the time step size on mass balance errors, as shown in Figures 5a, 5c, and 5e, where subsurface, surface, and coupling errors obtained for the sloping plane using a horizontal

Table 2. Parameter Values for the Test Cases

Variable	Units	Sloping Plane	Tilted v-Catchment	Enza River Drainage Basin
Horizontal mesh resolution	m	5,10,20,40,80	15,25,75	90,180,360
Time step size	s	15,30,60	30,60,150	600,1800,3600
Manning for hillslope	m ^{-1/3} s	0.02	0.5	0.5 ^a
Manning for channel	m ^{-1/3} s		0.02	0.05 ^a
Bedrock depth	m	5	5	150
Number of subsurface layers		25	16	19
Layer thickness (top to bottom)	m	0.2 (all layers)	0.05,0.05,0.05,0.05,0.05, 0.10,0.15,0.20,0.25,0.30, 0.35,0.40,0.50,0.60,0.80,	0.2,0.4,0.6,1.0,2.0,2.4, 3.0,4.0,5.0,6.4,8.0,10.0, 12.0,15.0,18.0,20.0,24.0,
Specific storage	m ⁻¹	5 × 10 ⁻⁴	5 × 10 ⁻⁴	5 × 10 ⁻⁴
Saturated hydraulic conductivity	mm h ⁻¹	4.164 × 10 ⁻¹	4.164 × 10 ⁻¹	3.6 × 10 ⁻¹ , 3.6 × 10 ⁻²
Initial water table depth	m	1.0	1.0	0.5
Rainfall rate	mm h ⁻¹	1.98 × 10 ¹	1.98 × 10 ¹	5.70 × 10 ⁻²
Evaporation rate	mm h ⁻¹	0.0	1.245 × 10 ⁻¹	2.85 × 10 ⁻²

^aVariable scaled upstream by using "at-a-station" relationship with exponents y' and b' equal to 0.33 and 0.2, respectively [Leopold and Maddock, 1953; Orlandini and Rosso, 1998; Camporese et al., 2010].

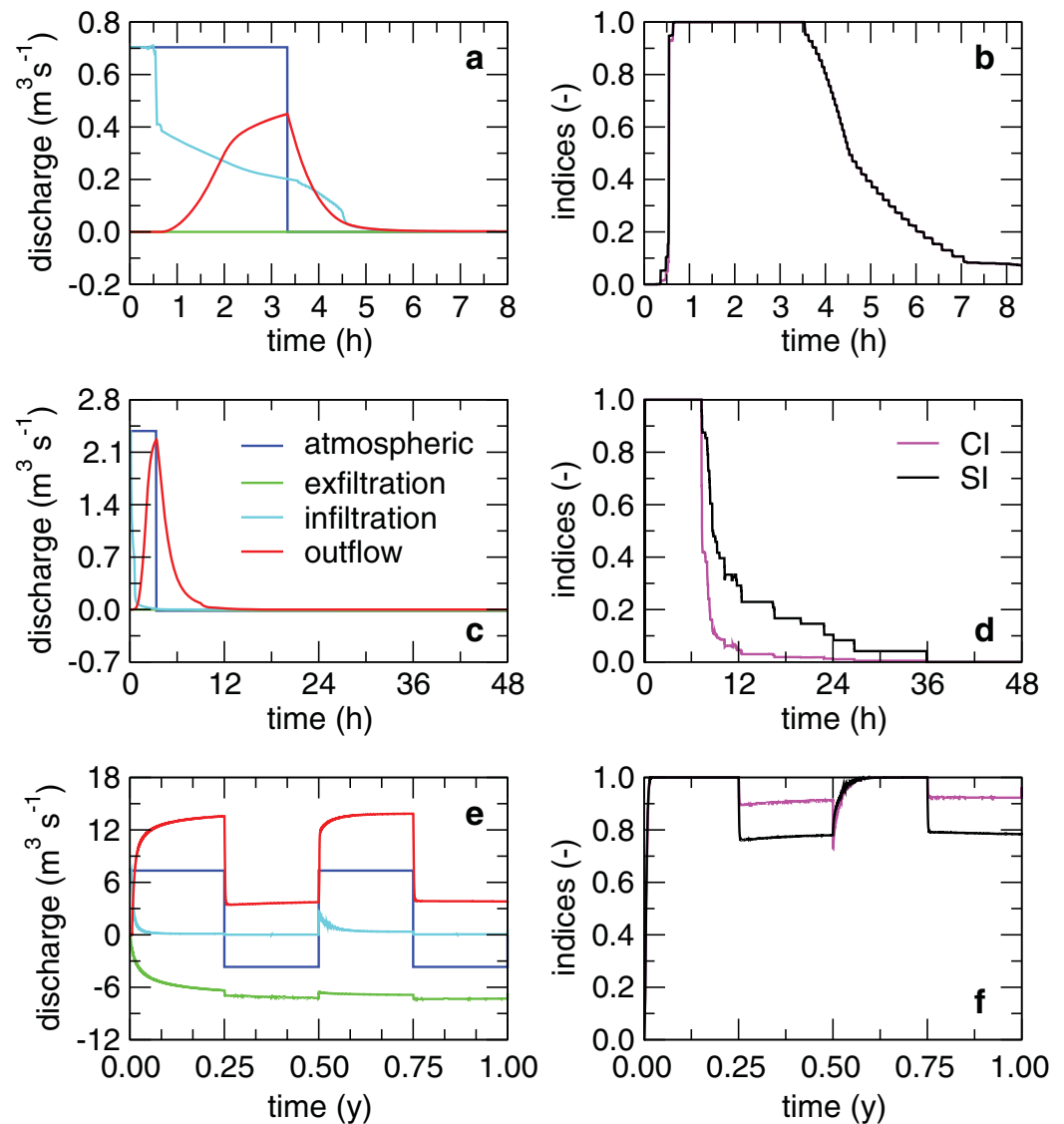


Figure 4. Examples of hydrological responses for (a, b) the sloping plane, (c, d) the tilted v-catchment, and (e, f) the Enza River drainage basin. Atmospheric, exfiltration, infiltration, and outflow discharges are shown in Figures 4a, 4c, and 4e, while saturation and degree of coupling indices are displayed in Figures 4b, 4d, and 4f.

mesh resolution of 10 m are reported. The subsurface error ϵ_{ssw} decreases as the time step gets smaller (Figure 5a), the surface error ϵ_{sw} increases slightly (Figure 5c), and the coupling mass balance error ϵ_c decreases (Figure 5e). Three different phases can be identified in the hydrological response of the sloping plane in Figure 4a: (1) transition from unsaturated to saturated conditions on the surface, (2) surface routing during a rising limb, and (3) surface routing during a recession limb. The first phase (from 0 to 0.65 h) is characterized by an increase of subsurface error due to the initial abrupt variation of atmospheric forcing. A similar behavior can be observed at 3.33 h for the same reason. The surface and coupling errors are null because the problem is uncoupled in this interval. Surface routing is activated during rainfall in the second phase (from 0.65 to 3.33 h), where the subsurface error decreases rapidly (Figure 5a) while surface and coupling errors rise (Figures 5c and 5e). During the final recession phase, there is first a rapid increase in surface error and a drop in coupling error when the rainfall stops (Figures 5c and 5e), followed by a period of stabilization of mass balance errors. The coupling error is clearly influenced by the time step size, as can be seen in Figure 5e where the slope and the drop of ϵ_c are proportional to Δt . As can be seen in Figure 5c, the connection between surface error and time step size is less direct, with this error influenced by transitions from unsaturated to saturated conditions (first and second phases) and vice versa (recession phase).

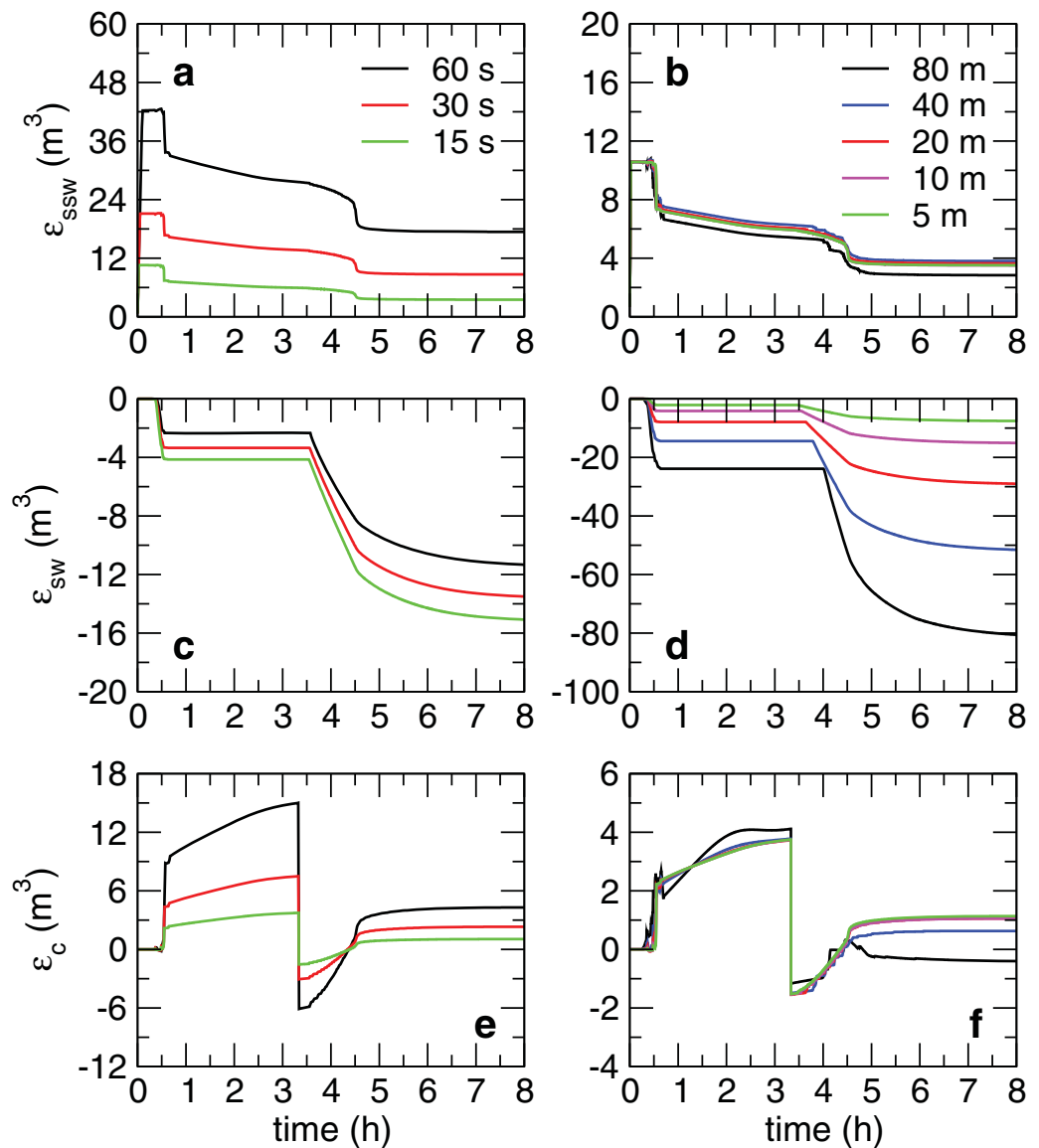


Figure 5. Sensitivity of subsurface, surface, and coupling (top to bottom) mass balance errors to temporal (a, c, e) and spatial (b, d, f) resolution for the sloping plane test case with a 10 m DEM.

5.1.2. Interpolation Algorithm

The influence of horizontal mesh size for the sloping plane is reported in Figures 5b, 5d, and 5f. The subsurface mass balance error ϵ_{ssw} is not significantly controlled by grid cell size (Figure 5b), while the surface error ϵ_{sw} is clearly affected by the mesh size, especially during the recession limb (Figure 5d). The coupling mass balance error ϵ_c displays a general insensitivity to horizontal mesh size, although a decrease in spurious oscillations as the mesh is refined can be noted in Figure 5f. When reducing the horizontal mesh size, exchange fluxes and surface water storage S_{sw} are better estimated in space, so that the volumetric flow rate to the surface Q_{sw} better matches the effective availability of surface cell water storage that passes from saturated to unsaturated conditions. Thus, a better evaluation of Q_{sw} and S_{sw} yields a decrease of ϵ_{sw} as shown in Figure 5d.

The spatial distribution of surface mass balance errors was studied in detail for the Enza River drainage basin. The ponding head h , the downstream discharge Q released from every cell, and the specific cell surface error associated to the i th cell $\epsilon_{cell}^{(i)}$ (equation (11)) are displayed in Figure 6 for three different horizontal mesh resolutions, namely 90, 180, and 360 m, at the same time $t^{(k+1)}$ of 10.5 months. The specific cell

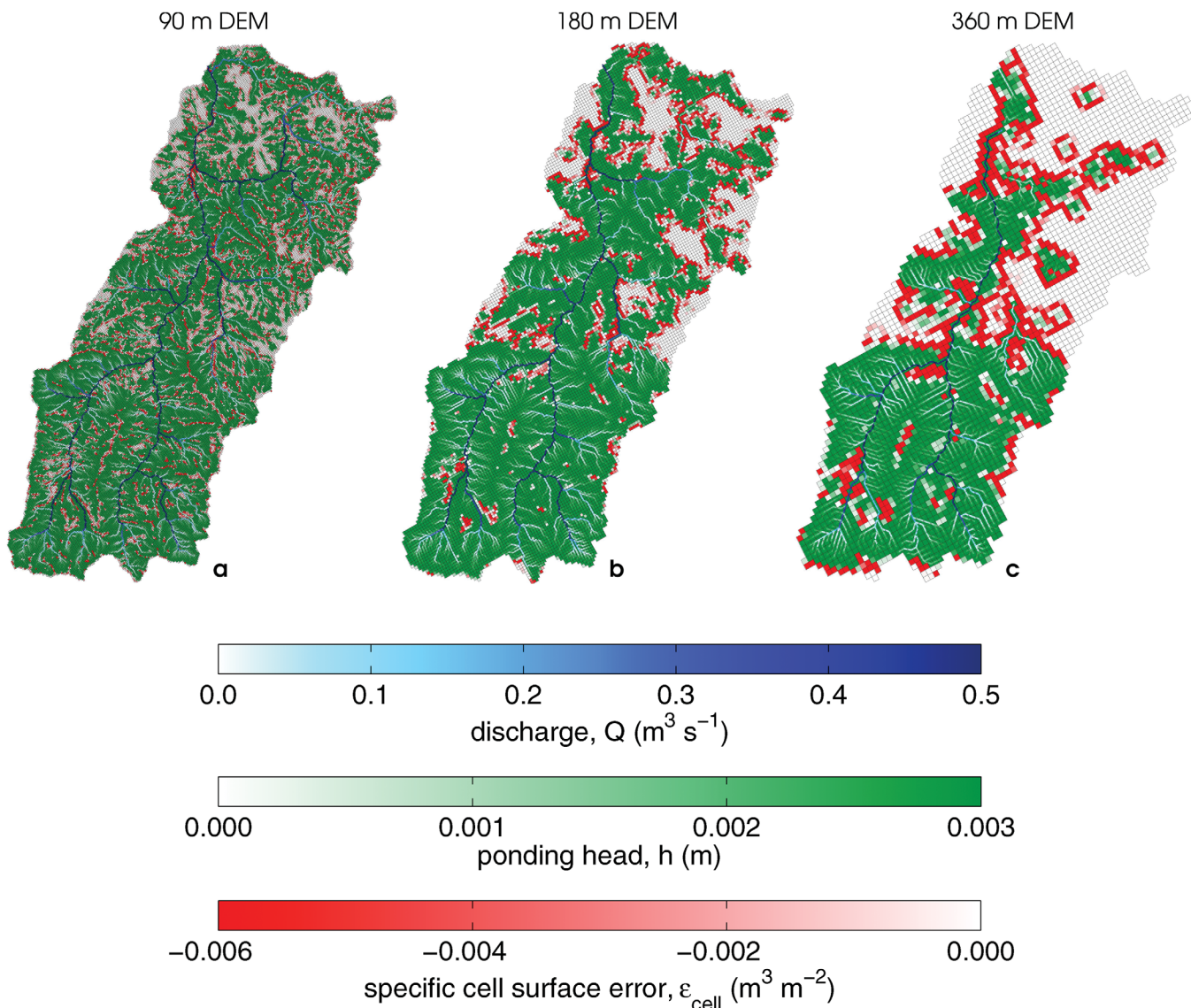


Figure 6. Spatial distribution of outflow discharge from surface cells Q , ponding head h , and specific cell surface error ϵ_{cell} for the Enza River drainage basin at horizontal mesh resolution (a) 90 m, (b) 180 m, and (c) 360 m, and at time 10.5 months. The time step size was 1800 s for all three runs.

surface error is not significantly controlled and influenced by surface routing along the drainage network, but ϵ_{cell} rises in all cells that are at the boundary between saturated and unsaturated zones, as can be seen by the red patches in Figure 6. The use of high mesh resolutions reduces the size of these patches and thus the magnitude of the related error. However, when large cells have to be used due to computational constraints, mass balance errors may be expected to arise when describing the transitions from saturated to unsaturated areas within a drainage basin. Since cells cannot contain negative surface water storages, a specific numerical strategy is needed to mitigate the mass balance errors during these critical transitions.

The global behavior of the drainage basin in terms of mass balance errors and outflow discharge is shown in Figure 7, where it can be seen that mesh refinement reduces the cumulative surface error ϵ_{swr} , especially during recession limbs. In contrast to the sloping plane test case, the geometric complexity of the Enza basin has a significant impact on subsurface error (Figure 7a). The coupling error is not strongly influenced by mesh resolution (Figure 7c), although higher mesh resolution produces smoother variations in ϵ_c . The Enza basin also displays different outflow responses for the different mesh element sizes, in particular for peak discharge and base flow (Figure 7d).

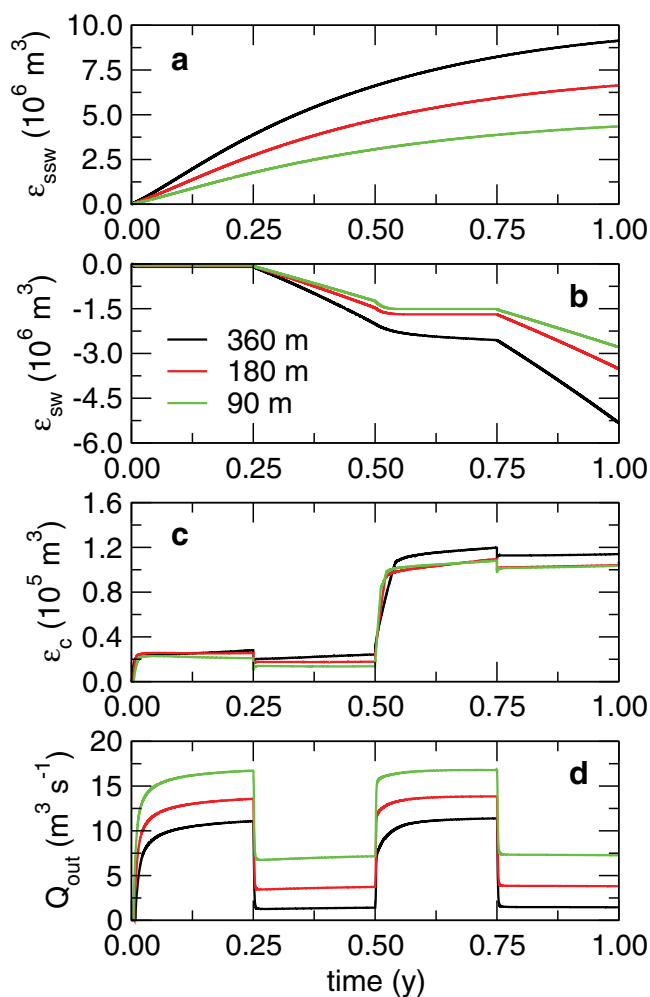


Figure 7. Sensitivity of cumulative mass balance errors (subsurface (a), surface (b), and coupling (c)) and outflow discharge (d) to grid cell size for the Enza River drainage basin. The time step size was 1800 s for all three runs.

5.2. Saturation and Coupling Indices

Saturation and coupling indices are introduced in order to track the sources of coupling error and the hydrologic interactions involved across the basin. In the example runs of Figure 4 for the three test cases, the sloping plane (Figures 4a and 4b) shows a case where CI closely follows SI during the recession limb because of a null atmospheric input. For the tilted v-catchment (Figures 4c and 4d), the saturation index is higher than the degree of coupling index due to a fast recession in the upper part of the basin that reduces significantly the exchange fluxes between the surface and subsurface domains. The exchange fluxes occurring over saturated areas, simulated by imposing Dirichlet boundary conditions, are significantly lower than the evaporation fluxes from unsaturated nodes across whole drainage basin. Under these conditions, the degree of coupling index displays low values. The Enza River drainage basin (Figures 4e and 4f) shows the opposite behavior because of the strong surface-subsurface interaction. Note that the degree of coupling index in Figure 4f drops when the transition from the first evaporation period to the second rainfall period occurs. This means that the exchange fluxes are preserved on saturated areas, while they increase significantly on unsaturated areas.

Saturation and coupling indices are examined as displayed in more detail for the tilted v-catchment in Figure 8. The surface error is influenced more by the horizontal mesh resolution than by the time step size as can be seen in Figures 8a and 8b. The reduction of time step size is shown in Figures 8a, 8c, and 8e. A similar hydrologic dynamics is described since smaller time step sizes determine a faster transition from saturated to unsaturated conditions during the recession limb (Figure 8c). Comparable surface errors are generated from configurations of the case study that present a similar behavior of saturation and coupling indices, namely for time step sizes of 30 and 60 s. The variation of horizontal mesh resolution is shown in Figures 8b, 8d, and 8f where the saturation index shows different patterns during the recession limb, with a smoother SI profile in the time interval (6.5 h, 24 h) when the mesh is refined. Similar behavior is obtained for the degree of coupling index. Note in Figure 8 that a change of SI implies a modification of exchanged fluxes, but a variation of CI can occur without a change in surface saturation. In addition, when the degree of coupling index is constant, the slope of surface error does not vary. In fact, if atmospheric boundary conditions from one time step to the next are not modified by the switching procedure, then exchange fluxes are maintained constant and the contribution of node-to-cell interpolation to surface error is unaltered.

5.3. Controlling Coupling Errors

Starting from the original CATHY code (“O” in Figures 9 and 10), three modifications are proposed to reduce mass balance errors: (1) a new time step size control by considering the variation of the degree of coupling index (“TC” in Figures 9 and 10); (2) an improved interpolation algorithm to pass exchange variables from

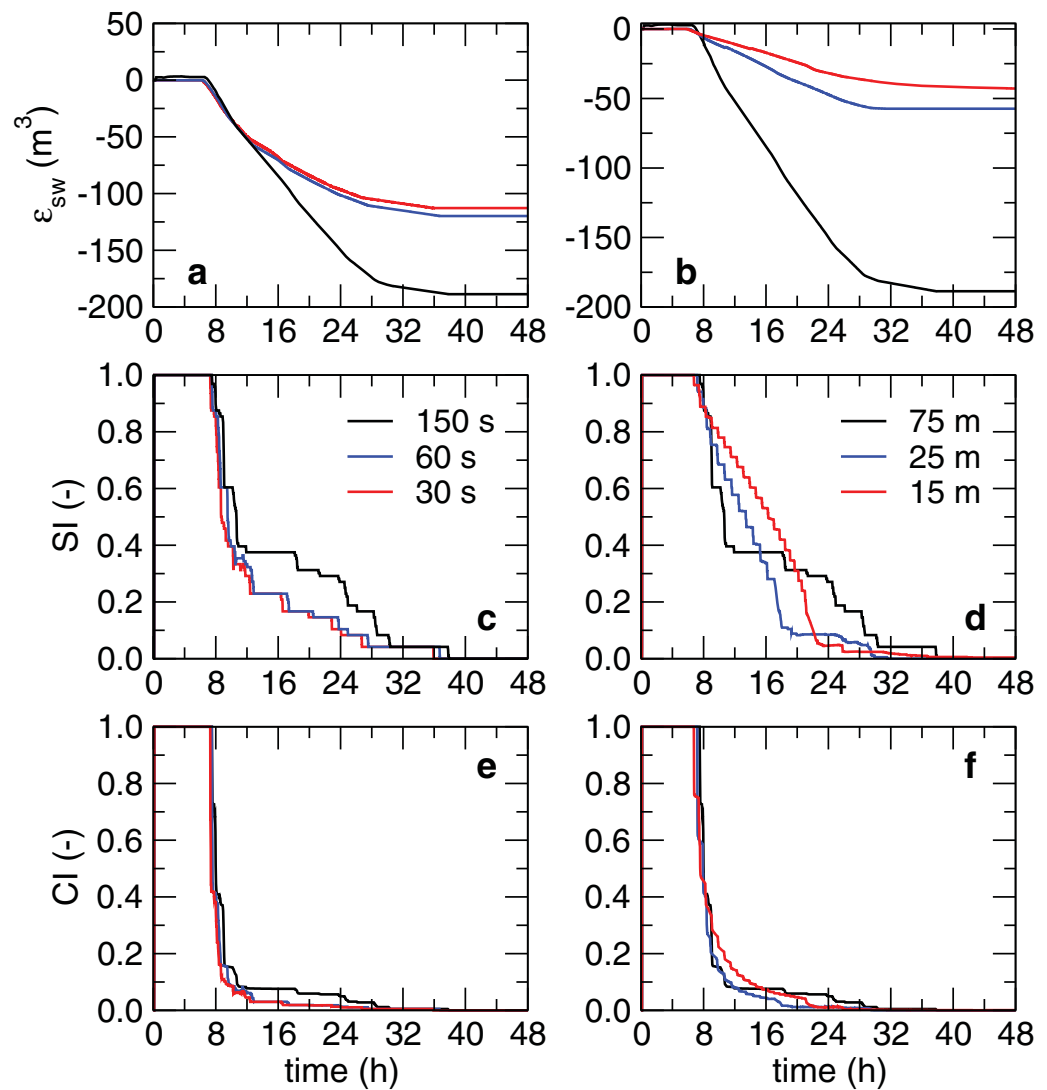


Figure 8. Sensitivity over time of surface error (a, b), saturation index (c, d), and coupling index (e, f) to time step size (a, c, e; horizontal mesh resolution is fixed at 75 m), and to grid cell size (b, d, f; time step size is fixed at 150 s) for the tilted v-catchment.

nodes to cells ("IA"); and (3) the combination of IA and TC ("IT"). The final values of subsurface, surface, and coupling cumulative mass balance errors are reported in Figure 9 for runs O, TC, IA, and IT. The time step size was varied in Figures 9a, 9c, and 9e for the sloping plane, tilted v-catchment, and Enza basin, respectively, while the horizontal mesh resolution was varied in Figures 9b, 9d, and 9f for the same sequence of test cases. The error magnitudes observed across the considered test cases are clearly affected by drainage basin size. For a given drainage basin, the sources of error are found to be essentially connected to (1) mesh size, (2) terrain complexity, and (3) rate of change in time of exchange fluxes at the land surface. In fact, the highest error magnitudes are observed for the Enza River drainage basin while the lowest are observed for the sloping plane (Figure 9). The mesh size is found to affect the magnitude of both subsurface and surface errors as shown, for instance, in the sloping plane and tilted v-catchment, where relatively large surface errors are obtained as compared to subsurface and coupling errors. Terrain complexity affects especially the magnitude of the subsurface error as shown, for instance, in the Enza River drainage basin. Finally, the rate of change in time of exchange fluxes is found to affect particularly the magnitude of the coupling error, as shown in the tilted v-catchment, where significant coupling errors (as compared to subsurface and surface errors) are generated by rapid transitions from saturated to unsaturated conditions due to the steep terrain slope.

The subsurface error is influenced by time step size as highlighted in Figure 9a, where ϵ_{SSW} decreases with step size. The modified versions of CATHY improve the subsurface mass balance error, in particular when the

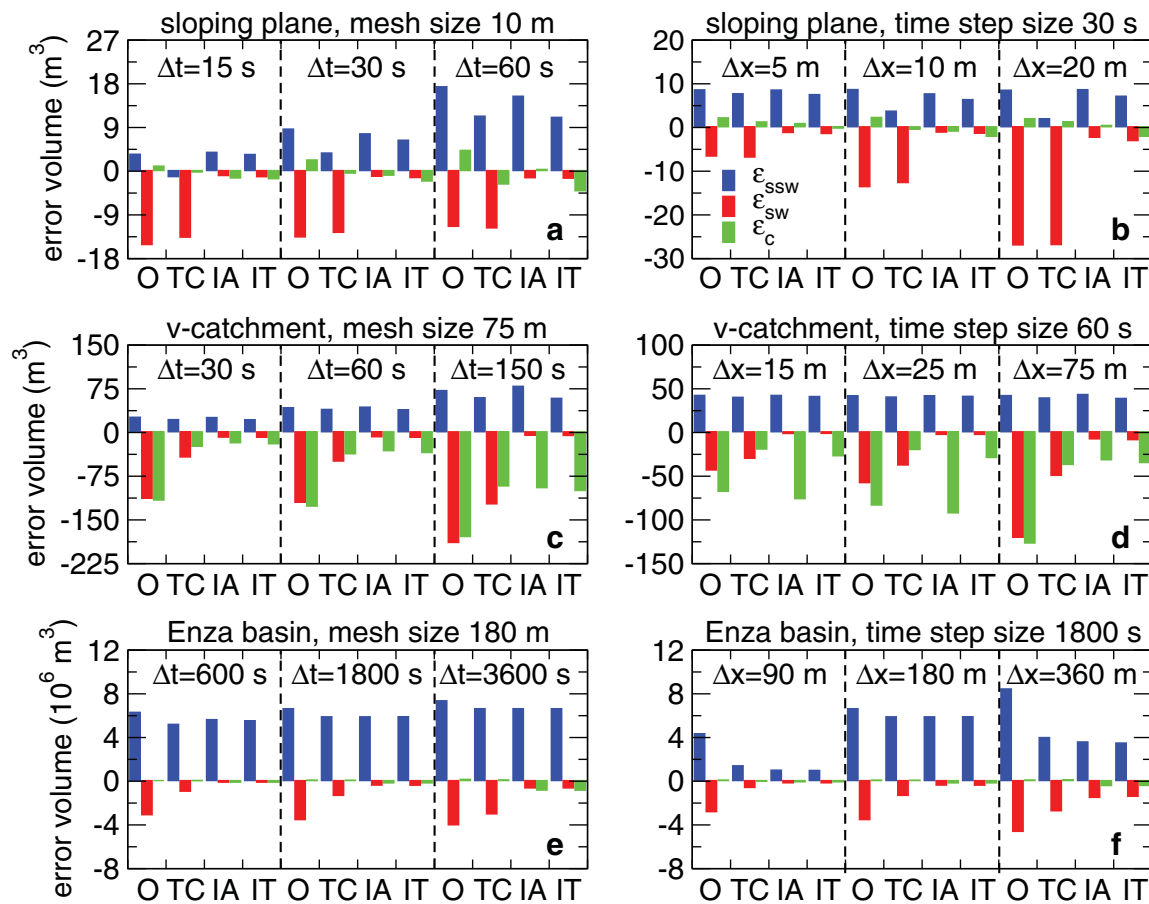


Figure 9. Histograms of cumulative volume errors for the sloping plane (a, b), tilted v-catchment (c, d), and Enza River drainage basin (e, f). Subsurface, surface, and coupling errors are represented in blue, red, and green, respectively. Four versions of CATHY are compared: original code (O), modified time step size control (TC), new interpolation algorithm for surface routing (IA), and combination of TC and IA (IT). The time step sizes (a, c, e) and horizontal mesh sizes (b, d, f) used for the different runs are shown in the graphs.

new time step size control is used. However, the decrease in subsurface error with time step size is less evident with more complex topography, as shown in Figure 9e for the Enza basin. The surface error is comparable or greater than the subsurface error in most of test cases considered, especially for the original code. Smaller time step size does not reduce the surface error for the sloping plane geometry, as shown in Figure 9a, while for the tilted v-catchment and Enza basin ϵ_{sw} decreases with Δt , as shown in Figures 9c and 9e. The surface error is clearly reduced in all test cases by considering the modification IA and IT with the improved interpolation algorithm. The coupling error is not as favorably impacted as surface error by the modified algorithms (Figures 9c and 9e), and in some cases ϵ_c even increases. The results obtained indicate that the surface-subsurface flow model accuracy increases when the dynamics of the simulated processes is monitored and representative indices are used to drive the adaptive time stepping. The proposed adaptive scheme does not degrade computational efficiency and may even enhance it by reducing the occurrence of failed time steps (which require the model to backstep, i.e., to redo the entire time step using a smaller time step size).

The horizontal mesh size does not significantly affect the subsurface error for simple and symmetric geometries, as shown in Figures 9b and 9d, while in a more complex test case, as the Enza basin, ϵ_{SSW} is improved when the mesh size is reduced (Figure 9f). The influence of modifications to CATHY for ϵ_{SSW} is not significant for the sloping plane and tilted v-catchment, while the subsurface error is improved for the Enza basin. The surface error is greatly affected by horizontal mesh size, as can be seen in Figure 9d, where surface error is reduced as the cell size decreases. The surface error is significantly reduced by using the modified versions IA and IT, where the interpolation algorithm decreases the errors highlighted in Figure 6 that are generated on boundaries between saturated and unsaturated cells. The coupling error is not significantly influenced by horizontal mesh size for the sloping plane and Enza basin (Figures 9b and 9f), while for the tilted v-

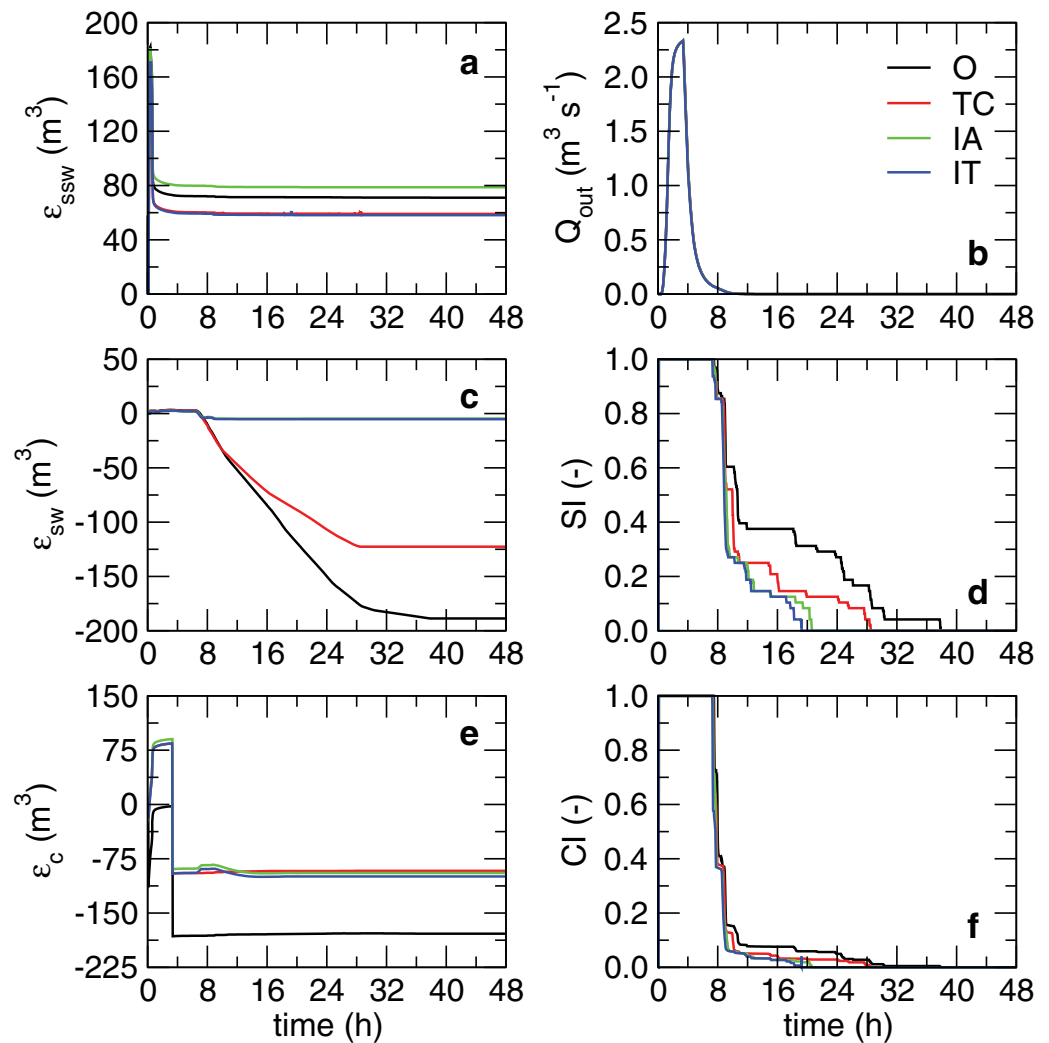


Figure 10. Subsurface error (a), outflow discharge (b), surface error (c), saturation index (d), coupling error (e), and coupling index (f) for the four CATHY versions (original code (O), modified time step size control (TC), new interpolation algorithm (IA), and combined TC and IA (IT)) for the tilted v-catchment. The time step size was 150 s and the horizontal mesh resolution was 75 m.

catchment ϵ_c is reduced as the mesh size decreases (Figure 9d). In general when the surface error is reduced by using the new interpolation algorithm, the coupling error increases slightly, but this is more than offset by the decrease in surface error. The results shown in Figures 6 and 9 indicate that the numerical schemes adopted to define the boundary conditions and to model exchange fluxes are especially important in describing accurately the transitions from saturated to unsaturated areas.

A detailed examination of a representative test case is presented in Figure 10, where a comparison of the four versions of CATHY (O, TC, IA, and IT) for the tilted v-catchment with a time step size of 150 s and a horizontal mesh size of 75 m is reported. The subsurface, surface, and coupling errors are shown, respectively, in Figures 10a, 10c, and 10e, the outflow discharge from the outlet is shown in Figure 10b, and the saturation and coupling degree indices are shown in Figures 10d and 10f, respectively. As demonstrated previously in Figures 5a and 9a, since the subsurface error is influenced by the time step size, ϵ_{SSW} is reduced by using the modified time step size control, either alone or in combination with the new interpolation algorithm (Figure 10a), but increases slightly if only IA is used. The surface error rises during the recession limb (Figure 10c), while ϵ_{SW} is stabilized when all surface nodes are unsaturated, as shown by the saturation index in Figure 10d. The surface error is reduced to 3% of the original code results by using the modified versions IA and IT. The coupling error rises rapidly during the saturation phase and drops at the end of the rainfall at time 3.33 h, as shown in Figure 10e. All the modified versions of CATHY improve ϵ_c to 50% of the original

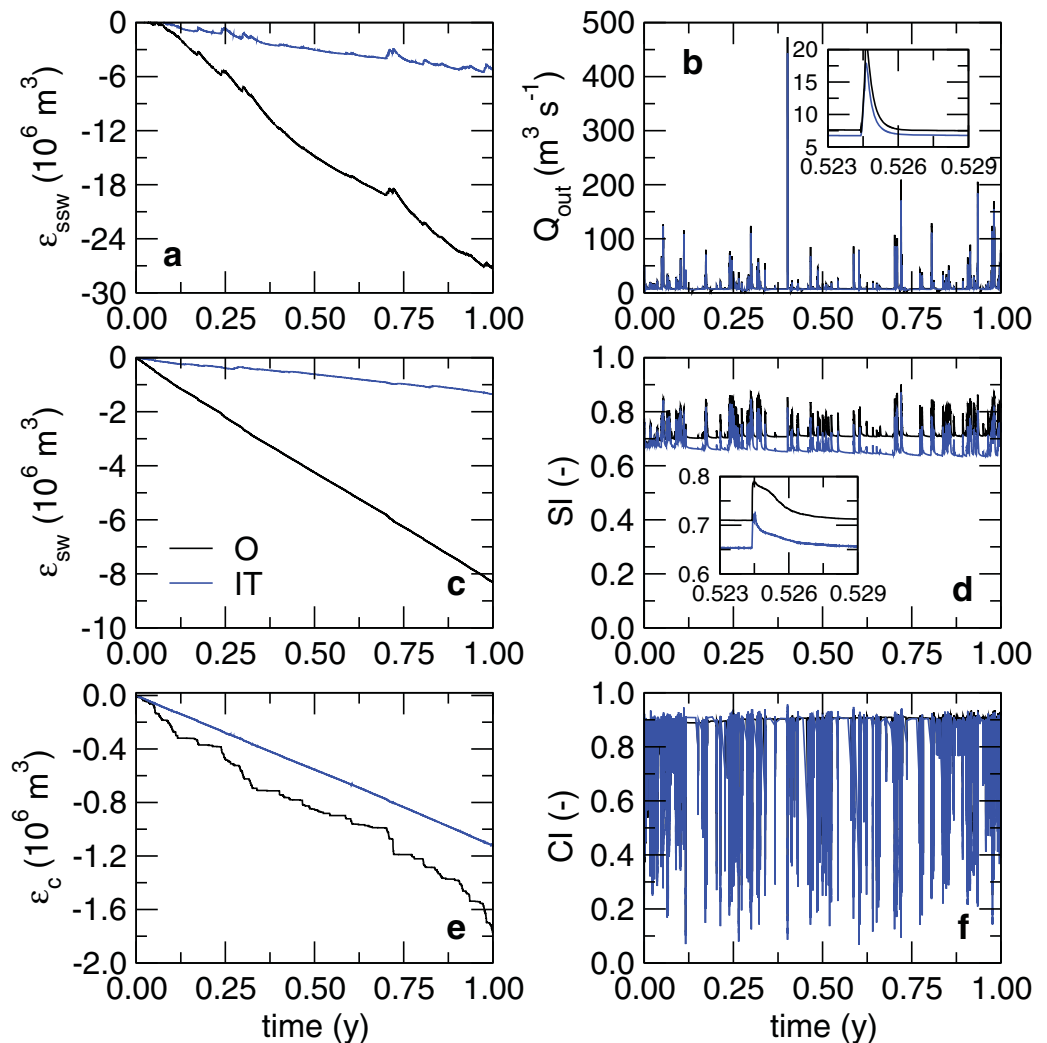


Figure 11. Subsurface error (a), outflow discharge (b), surface error (c), saturation index (d), coupling error (e), and coupling index (f) for two CATHY versions (original code (O) and combined TC and IA codes (IT)) for the Enza River drainage basin responding to real atmospheric forcing for the year 2009. The time step size was 1800 s and the horizontal mesh resolution was 180 m.

value. The outflow hydrographs shown in Figure 10b are indistinguishable for the four code versions, which is reassuring. However, the saturation index in Figure 10d displays different behaviors at the end of the recession. Surface saturation for the original code (case O) falls to zero at time 37.9 h, while for the modified versions of CATHY this occurs earlier (at times 28.5, 20.6, and 19.2 h for TC, IA, and IT, respectively). A similar behavior is observed in Figure 10f for the coupling degree index. The modified versions ensure a faster transition from saturated to unsaturated conditions and reduce the mass balance errors, especially ϵ_{SW} .

Finally, to evaluate the impact of the proposed error mitigation strategy on the long-term response of a real drainage basin, the Enza River drainage basin was simulated for the year 2009 (Figure 11). Net atmospheric forcing (rainfall minus evaporative demand) was assigned to each land surface node using data from the nearest weather station. The outflow hydrographs were computed for both the O and IT codes (Figure 11b). The subsurface and surface errors are significantly reduced, as shown in Figures 11a and 11c, respectively, whereas the coupling error is not greatly affected (Figure 11e). The improvement for the IT code is particularly evident in the recession limbs (inset in Figure 11b). This may be connected to the improved description of surface saturation, as indicated by the saturated area index plotted in Figure 11d. The degree of coupling index displays significantly higher oscillations in the real case of the Enza River drainage basin (Figure 11f) than in the synthetic cases (compare for instance Figure 10f). This is likely due to the greater variability in atmospheric forcing when using real data over long-time periods. The reduction in surface mass balance

error obtained for the IT version over the O code has a significant impact on the relative magnitudes of subsurface, surface, and coupling errors (Figure 11a, 11c, and 11e). The water budget has been globally improved by the new interpolation scheme with the reduction of surface error (Figure 11c).

6. Conclusions

An in-depth analysis of the sources of mass balance error in sequential iterative surface-subsurface flow models was performed. The different sources were investigated by isolating subsurface, surface, and coupling errors and by using a saturation area index and a coupling degree index to track these errors. The analyses were performed for two synthetic test cases and a complex drainage basin in northern Italy simulated by the CATHY model. A modified time step control scheme was introduced to improve model performance by considering a normalized variation of the coupling index. The node-to-cell interpolation of the exchange fluxes between the surface and subsurface grids was also found to be critical. A detailed analysis of the spatial distribution of surface error on each cell revealed that the main source of surface error arises in cells that are in transition between saturated and unsaturated state, rather than along the drainage network where the area is normally saturated. A new interpolation algorithm was therefore developed that considers the availability of water on surface cells and thus improves the description of subsurface-surface interaction. This enhancement resulted in significantly reduced surface mass balance error, in particular during recession phases.

Although this work was focused on a specific model, it highlights general aspects that need to be considered when evaluating the performance of surface-subsurface flow interaction models. It has been demonstrated that sources of error can be identified and controlled by monitoring the temporal and spatial mass balance behavior and by using dimensionless indices to determine suitable time steps for each phase of the simulation period. The results show that the time stepping scheme and interpolation algorithm for the surface-subsurface interface grid are pivotal for the performance of the model. When a sequential time stepping scheme is used, which has computational advantages over other approaches, a time lag between the surface and subsurface domains is introduced and a coupling error is generated. This error can be controlled, however, by adapting the time interval when the dynamics of the drainage basin requires a smaller time scale because of the rapid variation of exchange fluxes through the land-atmosphere interface. This can be implemented by using an dimensionless index such as the degree of coupling index presented in this study. The geometric interpolation of variables from one computational grid onto another introduces mass balance errors that in general depend on the mesh resolution and the dynamics involved. The interpolation algorithm used at the surface-subsurface interface to pass exchange fluxes is therefore critical in coupled numerical models, especially when some variables are constrained to assume nonnegative values, such as the cell surface water storage or the outflow from unsaturated cells. This issue can be mitigated by using a suitable algorithm to interpolate exchange fluxes, as shown in this work. The analysis performed here for one class of coupling approaches (sequential iterative) can be usefully applied to other approaches used in integrated surface-subsurface flow models, to shed light on the comparative mass balance performance of these models.

Acknowledgments

This study was carried out under the research program PRIN 2010–2011 (grant 2010JHF437) funded by the Italian Ministry of Education, University, and Research. The Regional Environmental Protection Agency of Emilia-Romagna (ARPA-ER, Bologna, Italy) and Iren SpA (Reggio Emilia, Italy) are acknowledged for providing the hydrological data for the Enza River drainage basin. The data in our article can be provided upon request to Marcello Fiorentini (marcello.fiorentini@unimore.it) or Stefano Orlandini (stefano.orlandini@unimore.it). The authors are grateful to the four anonymous reviewers for comments that led to improvements in the manuscript.

References

- Aricó, C., M. Sinagra, L. Begnudelli, and T. Tucciarelli (2011), MAST-2D diffusive model for flood prediction on domains with triangular Delaunay unstructured meshes, *Adv. Water Resour.*, *34*, 1427–1449, doi:10.1016/j.advwatres.2011.08.002.
- Camporese, M., C. Paniconi, M. Putti, and S. Orlandini (2010), Surface-subsurface flow modeling with path-based runoff routing, boundary condition-based coupling, and assimilation of multisource observation data, *Water Resour. Res.*, *46*, W02512, doi:10.1029/2008WR007536.
- Camporese, M., E. Daly, P. E. Dresel, and J. A. Webb (2014), Simplified modeling of catchment-scale evapotranspiration via boundary condition switching, *Adv. Water Resour.*, *69*, 95–105, doi:10.1016/j.advwatres.2014.04.008.
- Dagès, C., C. Paniconi, and M. Sulis (2012), Analysis of coupling errors in a physically-based integrated surface water-groundwater model, *Adv. Water Resour.*, *49*, 86–96, doi:10.1016/j.advwatres.2012.07.019.
- Delfs, J.-O., C.-H. Park, and O. Kolditz (2009), A sensitivity analysis of Hortonian flow, *Adv. Water Resour.*, *32*(9), 1386–1395, doi:10.1016/j.advwatres.2009.06.005.
- Ebel, B. A., B. B. Mirus, C. S. Heppner, J. E. VanderKwaak, and K. Loague (2009), First-order exchange coefficient coupling for simulating surface water-groundwater interactions: Parameter sensitivity and consistency with a physics-based approach, *Hydrol. Processes*, *23*, 1949–1959, doi:10.1002/hyp.7279.
- Freeze, R. A., and R. L. Harlan (1969), Blueprint for a physically-based, digitally-simulated hydrologic response model, *J. Hydrol.*, *9*, 237–258.
- Furman, A. (2008), Modeling coupled surface-subsurface flow processes: A review, *Vadose Zone J.*, *7*, 741–756, doi:10.2136/vzj2007.0065.
- Goumiri, I. R., and J. H. Prevost (2011), Cell to node projections: An assessment of error, *Int. J. Numer. Anal. Methods Geomech.*, *35*, 837–845, doi:10.1002/nag.927.
- Ivanov, V. Y., E. R. Vivoni, R. L. Bras, and D. Entekhabi (2004), Catchment hydrologic response with a fully distributed triangulated irregular network model, *Water Resour. Res.*, *40*, W11102, doi:10.1029/2004WR003218.

- Kampf, S. K., and S. J. Burges (2007), A framework for classifying and comparing distributed hillslope and catchment hydrologic models, *Water Resour. Res.*, *43*, W05423, doi:10.1029/2006WR005370.
- Kollet, S. J., and R. M. Maxwell (2006), Integrated surface groundwater flow modeling: A free-surface overland flow boundary condition in a parallel groundwater flow model, *Adv. Water Resour.*, *29*, 945–958.
- Leopold, L. B., and T. Maddock Jr. (1953), The hydraulic geometry of stream channels and some physiographic implications, *U.S. Geol. Surv. Prof. Pap.* 252, 57 pp.
- Liggett, J. E., A. D. Werner, and C. T. Simmons (2012), Influence of the first-order exchange coefficient on simulation of coupled surface–subsurface flow, *J. Hydrol.*, *414–415*, 503–515, doi:10.1016/j.jhydrol.2011.11.028.
- Maxwell, R. M., and N. L. Miller (2005), Development of a coupled land surface and groundwater model, *J. Meteorol.*, *6*, 233–247, doi:10.1175/JHM422.1.
- Maxwell, R. M., et al. (2014), Surface–subsurface model intercomparison: A first set of benchmark results to diagnose integrated hydrology and feedbacks, *Water Resour. Res.*, *50*, 1531–1549, doi:10.1002/2013WR013725.
- Niu, G.-Y., et al. (2014), Incipient subsurface heterogeneity and its effect on overland flow generation: Insight from a modeling study of the first experiment at the Biosphere 2 Landscape Evolution Observatory, *Hydrol. Earth Syst. Sci.*, *18*, 1873–1883, doi:10.5194/hess-18-1873-2014.
- Orlandini, S., and G. Moretti (2009), Determination of surface flow paths from gridded elevation data, *Water Resour. Res.*, *45*, W03417, doi:10.1029/2008WR007099.
- Orlandini, S., and R. Rosso (1996), Diffusion wave modeling of distributed catchment dynamics, *J. Hydrol. Eng.*, *1*, 103–113.
- Orlandini, S., and R. Rosso (1998), Parameterization of stream channel geometry in the distributed modeling of catchment dynamics, *Water Resour. Res.*, *34*, 1971–1985.
- Orlandini, S., G. Moretti, M. Franchini, B. Aldighieri, and B. Testa (2003), Path-based methods for the determination of nondispersive drainage directions in grid-based digital elevation models, *Water Resour. Res.*, *39*(6), 1144, doi:10.1029/2002WR001639.
- Orlandini, S., G. Moretti, M. A. Corticelli, P. E. Santangelo, A. Capra, R. Rivola, and J. D. Albertson (2012), Evaluation of flow direction methods against field observations of overland flow dispersion, *Water Resour. Res.*, *48*, W10523, doi:10.1029/2012WR012067.
- Orlandini, S., G. Moretti, and A. Gavioli (2014), Analytical basis for determining slope lines in grid digital elevation models, *Water Resour. Res.*, *50*, 526–539, doi:10.1002/2013WR014606.
- Panday, S., and P. S. Huyakorn (2004), A fully coupled physically-based spatially-distributed model for evaluating surface/subsurface flow, *Adv. Water Resour.*, *27*, 361–382, doi:10.1016/j.advwatres.2004.02.016.
- Paniconi, C., and M. Putti (1994), A comparison of Picard and Newton iteration in the numerical solution of multi-dimensional variably saturated flow problems, *Water Resour. Res.*, *30*, 3357–3374.
- Paniconi, C., and E. F. Wood (1993), A detailed model for simulation of catchment scale subsurface hydrologic processes, *Water Resour. Res.*, *29*, 1601–1620.
- Ponce, V. M. (1986), Diffusion wave modeling of catchment dynamics, *J. Hydraul. Eng. Am. Soc. Civ. Eng.*, *112*, 716–727.
- Sebben, M. L., A. D. Werner, J. E. Liggett, D. Partington, and C. T. Simmons (2013), On the testing of fully integrated surface–subsurface hydrological models, *Hydrol. Processes*, *27*, 1276–1285, doi:10.1002/hyp.9630.
- Shen, C., and M. S. Phanikumar (2010), A process-based, distributed hydrologic model based on a large-scale method for surface–subsurface coupling, *Adv. Water Resour.*, *33*, 1524–1541, doi:10.1016/j.advwatres.2010.09.002.
- Sulis, M., S. B. Meyerhoff, C. Paniconi, R. M. Maxwell, M. Putti, and S. J. Kollet (2010), A comparison of two physics-based numerical models for simulating surface water–groundwater interactions, *Adv. Water Resour.*, *33*, 456–467, doi:10.1016/j.advwatres.2010.01.010.
- Sulis, M., C. Paniconi, C. Rivard, R. Harvey, and D. Chaumont (2011), Assessment of climate change impacts at the catchment scale with a detailed hydrological model of surface–subsurface interactions and comparison with a land surface model, *Water Resour. Res.*, *47*, W01513, doi:10.1029/2010WR009167.
- Syriopoulou, D., and A. D. Koussis (1991), Two-dimensional modeling of advection-dominated solute transport in groundwater by matched artificial dispersivity method, *Water Resour. Res.*, *27*, 865–872.
- van Genuchten, M. T., and D. R. Nielsen (1985), On describing and predicting the hydraulic properties of unsaturated soils, *Ann. Geophys.*, *3*, 615–628.
- VanderKwaak, J. E., and K. Loague (2001), Hydrologic-response simulations for the R-5 catchment with a comprehensive physics-based model, *Water Resour. Res.*, *37*, 999–1013.
- Weill, S., M. Altissimo, G. Cassiani, R. Deiana, M. Marani, and M. Putti (2013), Saturated area dynamics and streamflow generation from coupled surface–subsurface simulations and field observations, *Adv. Water Resour.*, *59*, 196–208, doi:10.1016/j.advwatres.2013.06.007.